International Journal of Microwave and Wireless Technologies

cambridge.org/mrf

6G upper mid-band independently controllable dual-polarized reconfigurable intelligent surface (RIS)

Mehmet Ahad Yurtoglu, Ramez Askar, Sven Wittig, Mathis Schmieder and Michael Peter

Fraunhofer Institute for Telecommunications, Heinrich Hertz Institute, HHI, Berlin, Germany

Research Paper

Cite this article: Yurtoglu MA, Askar R, Wittig S, Schmieder M, Peter M (2026) 6G upper mid-band independently controllable dual-polarized reconfigurable intelligent surface (RIS). *International Journal of Microwave and Wireless Technologies*, 1–13. https://doi.org/10.1017/S1759078726103341

Received: 31 December 2025
Revised: 7 May 2026
Accepted: 8 May 2026

Keywords:
Reconfigurable Intelligent Surface (RIS); Dual Polarization; Beam Steering; Varactor Diodes; Cross-Polarization Isolation; Bistatic Radar Cross Section (RCS); Monostatic Radar Cross Section (RCS); 6G Communications; Full-Duplex Communications; Integrated Sensing and Communication (ISAC)

Corresponding author:
Mehmet Ahad Yurtoglu;
Email: mehmet.ahad.yurtoglu@hhi.fraunhofer.de

Abstract

This paper presents a novel, independently controllable dual-polarized reconfigurable intelligent surface (RIS) unit cell for 6G upper mid-band (7.125–24.25 GHz) applications. The proposed unit cell is based on the diagonal placement of mutually orthogonal tunable radiators (loaded with varactor diodes) alongside static dual-polarized radiators. Full-wave electromagnetic simulations of the unit cell demonstrate a phase shift range of 270°, a maximum reflection loss of 4.5 dB, and 61 dB cross-polarization isolation (XPI) within a 400 MHz frequency range centered at 15 GHz. Furthermore, full-wave simulations of a 16×16 RIS panel were conducted for various reflection angles under both TE- and TM-polarized illuminations. The results demonstrate a wide-angle beam-steering capability of $\pm 60°$, with a maximum beam-pointing error of only 1.7°. The proposed RIS also exhibits accurate and stable reflection control under wide-angle excitation. A 3×3 prototype was fabricated to validate the unit cell's performance. Measurement results agree with the simulations, yielding a 270° phase shift, approximately 7 dB reflection loss, and 24 dB XPI. The proposed RIS is a promising candidate for future 6G communication systems.

Introduction

The transition from fifth-generation (5G) to sixth-generation (6G) wireless/mobile networks, or more precisely, the enhancement of 5G through the incorporation of advanced 6G technologies, necessitates a significant commitment in terms of effort and investment. Experts have projected that 6G will be allocated within the upper mid-range spectrum. In this context, leveraging the existing below-6-GHz mobile cell infrastructure, the new frequency bands must contend with increased path loss and more challenging propagation conditions. Furthermore, 6G aspires to substantially broaden coverage for non-terrestrial links, which are similarly affected by heightened propagation losses. As a result, the implementation of reconfigurable intelligent surfaces (RISs) emerges as a promising strategy to enhance link performance within 6G mobile networks [1].

An RIS can manipulate the phase of incident electromagnetic waves through its programmable elements, thereby steering reflected signals toward desired directions. This capability enables non-line-of-sight links to be effectively transformed into virtual line-of-sight paths via controlled reflections [2]. In full-duplex communication scenarios, RISs are required to support dual polarization, as simultaneous transmission and reception often rely on two orthogonal polarization channels to improve self-interference cancellation (SIC) [3]. Moreover, dual-polarized RIS architectures are particularly attractive for Integrated Sensing and Communication (ISAC) systems [4], which represent a key pillar of 6G networks. For such applications, the most critical design requirements include minimal polarization conversion – equivalently, high cross-polarization isolation (XPI) – and independent control over both polarization channels [5]. High isolation ensures interference-free operation between polarization channels, thereby enhancing both communication reliability and sensing performance.

In recent years, dual-polarized RISs have been extensively investigated using various phase-shifting technologies, including liquid crystal [6], positive-intrinsic-negative (PIN) diodes [7–11], and varactor diodes [12–14]. Several design strategies have been proposed in the literature to enhance the XPI. In [9], orthogonally arranged dipoles combined with a crossover structure are employed, resulting in an XPI improvement up to 25 dB. A cross-shaped slot integrated into the main radiator is used in [11] to suppress cross-polarized components, achieving an XPI of approximately 30 dB. A 180° hybrid coupler placed in the middle layer of a guided-wave-inspired structure provides

© The Author(s), 2026. Published by Cambridge University Press in association with The European Microwave Association. This is an Open Access article, distributed under the terms of the Creative Commons Attribution-NonCommercial licence (http://creativecommons.org/licenses/by-nc/4.0), which permits non-commercial re-use, distribution, and reproduction in any medium, provided the original article is properly cited. The written permission of Cambridge University Press or the rights holder(s) must be obtained prior to any commercial use.

an XPI level of 23 dB. In [12], a modified particle swarm optimization algorithm is adopted to maximize XPI, yielding an isolation level of about 20 dB.

In this study, one of the SIC techniques – antenna passive cancellation based on polarization mutual orthogonality [15, 16] – is employed to enhance the XPI by utilizing a diagonal unit-cell topology. The unit cell is designed to operate in the upper mid-band (7.125–24.25 GHz), as this band is considered a strong candidate for 6G systems due to the limited data rates achievable in Frequency Range 1 (FR1, below 7.125 GHz) and the high propagation losses associated with Frequency Range 2 (FR2, 24.25–52.6 GHz). Consequently, the upper mid-band offers a favorable balance between bandwidth availability and propagation characteristics. The simulated and measured results show that the unit cell achieves a phase shift range of 270° at the center frequency of 15 GHz and exhibits high cross-polarization suppression performance, while requiring a minimal number of phase-tuning components (i.e., two varactor diodes per cell) compared with existing RIS designs.

An earlier version of this paper was presented at EuMW 2025 and was published in its Proceedings [17]. This journal builds upon the preliminary study by providing a comprehensive and systematic analysis of the proposed unit-cell architecture, detailed RIS simulations, and reflection-coefficient measurements of a fabricated prototype. The remainder of this paper is organized as follows. The second section describes the proposed unit-cell topology and explains its operational principles. The third section presents the RIS simulations under both normal and oblique incidence. The fourth section details the experimental validation of the unit cell. Finally, the fifth section provides the concluding remarks.

Unit cell design and simulation

Topology

As previously mentioned, the RIS can employ dual-polarization capability with high XPI, enabling its use in full-duplex or ISAC systems. Therefore, the unit cell of the RIS must also be dual-polarized, and the reflection phase of each polarization state must be controlled independently. To minimize the complexity of the reflection-phase control, the unit-cell behavior should remain as similar as possible for both polarizations. Considering the scalability requirements of the RIS, the number of phase-tuning components per unit cell must be kept to a minimum to reduce overall cost.

Using a single varactor diode might be sufficient to realize a dual-polarized cell [18]; however, the reflection-phase control would then be joint, meaning the reflection phases of the two polarizations could not be tuned independently. Moreover, the cell's reflection characteristics may vary with polarization. Thus, achieving independent control for both polarization states requires at least two varactor or PIN diodes. A geometric constraint of using two diodes is that they cannot be placed at the center of the unit cell, as they would physically overlap. To address this, a radiator can be positioned at the center, with two parasitic elements placed at the edges and connected to the main radiator via diodes [7, 12]. With this configuration, both polarization states can be controlled independently while maintaining the minimum number of diodes. However, because both polarizations share the same main radiator, the XPI may not be sufficiently high for full-duplex or ISAC applications. To increase XPI while preserving independent controllability and keeping the number of varactors at a minimum, the radiators for each polarization can be separated and placed side by side [19]. A similar approach, which overlaps vertically and horizontally polarized unit cells to realize a dual-polarized configuration, is presented in [20]. To ensure half-wavelength spacing between same-polarization radiators and to minimize inter-element coupling, we propose a diagonal unit-cell topology, as shown in Fig. 1(a). In this topology, the vertically polarized and horizontally polarized radiators are positioned diagonally, each occupying a quarter-wavelength sub-cell, while the overall unit-cell size remains half a wavelength. Additionally, two dummy dual-polarized radiators can be placed on the opposite diagonal to reduce reflection loss, as they also contribute to radiation for both polarization states. Note that the vertical and horizontal radiators are the ones independently controlled via varactors. Since they are spatially separated and mutually orthogonal, the XPI level can be further improved. A diagonal arrangement of vertically and horizontally polarized elements is also presented in [21], although it is intended for fixed or static (non-reconfigurable) RIS applications.

Design

Figure 1(b) shows the structure of the dual-polarized unit cell based on varactor diodes and the topology described in the previous section. The size of the unit cell is 10 mm × 10 mm ($p \approx \lambda_0/2$ at 15 GHz). The horizontally and vertically oriented bow-tie elements serve as controllable horizontally and vertically polarized radiators, while the square patches serve as dummy dual-polarized radiators. Slots are introduced into the bow-tie elements to reduce their electrical size without changing their resonant frequency, thereby enabling them to fit within the quarter-wavelength sub-cell. In addition, square-ring structures are placed around the bow-tie elements, as they modify the slope of the phase curve and enhance the phase-shift range, similar to the effect of an annular ring [22]. Vertical interconnect access (via) holes are placed to bias the varactor diodes with DC voltages.

Figure 1(c) illustrates the layer structure of the unit cell, which consists of three dielectric layers and four metallic layers. The top and bottom substrates are Rogers RO4350B ($\epsilon_r = 3.66$, $\tan\delta = 0.004$, $h_1 = h_3 = 0.762$ mm). These substrates are bonded using Rogers RO4450F ($\epsilon_r = 3.52$, $\tan\delta = 0.004$, $h_2 = 0.1$ mm), which serves as the middle dielectric layer. The bottom side of the top substrate is a fully metalized ground plane, except for the clearances around the via holes. The vias in the top substrate connect the bow-tie arms, and their associated varactor-diode pads, to the top metallic layer of the bottom substrate, which acts as a filtering layer. A radial stub is implemented on this layer to suppress or minimize RF current leakage before the signal is passed to the bottom layer, which contains all DC routing lines. Without this filtering stage, the RF power could couple into the DC supply network, potentially causing damage. Table 1 lists the dimensions of the proposed unit cell.

Analysis

Electromagnetic simulations of the proposed unit cell were performed in ANSYS® HFSS™ (High-Frequency Structure Simulator) using a Floquet port excitation placed on top of the air box. Two modes (TE, TM) were assigned to the Floquet port (see Fig. 1(b)). In the given coordinate system, the TE mode excites the vertically

https://doi.org/10.1017/S1759078726103341 Published online by Cambridge University Press

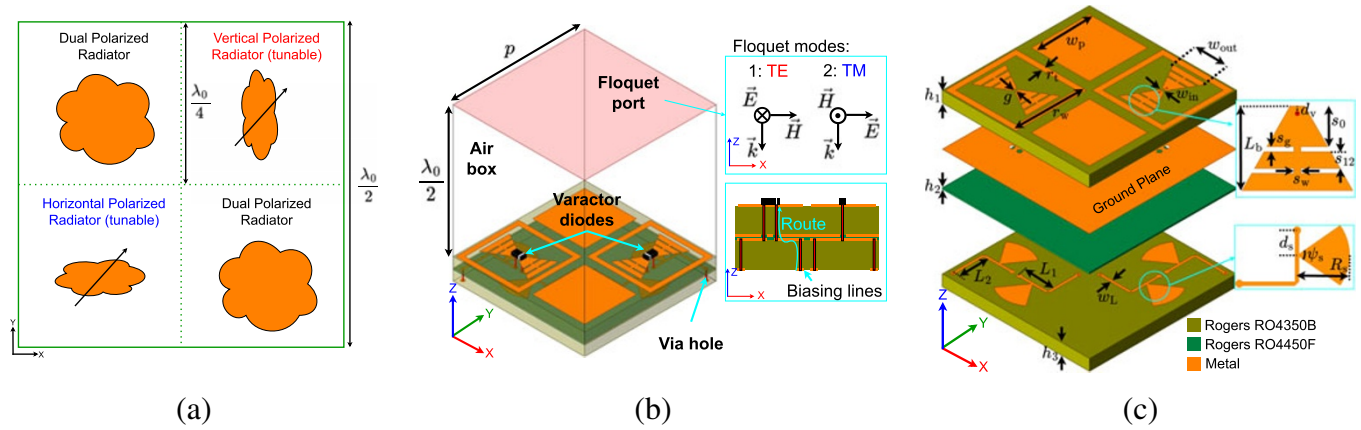


Figure 1. Unit cell configuration and design: (a) topology, (b) perspective view, and (c) expanded layers of the structure.

Table 1. Unit cell dimensions

Parameter	Substrate				Square ring and patch			Bow-tie				
	h_1	h_2	h_3	p	r_t	r_w	w_p	w_{in}	w_{out}	L_b	g	d_v
Value/mm	0.762	0.1	0.762	10	0.35	4.8	3.95	0.3	2.3	1.76	0.18	0.16
Parameter	Slots on bow-tie				Line and radial stub							
	s_0	s_{12}	s_w	s_g	w_L	L_1	L_2	d_s	R_s	ψ_s		
Value and unit	0.85 mm	0.35 mm	0.15 mm	0.1 mm	0.15 mm	2 mm	2 mm	0.9 mm	1.9 mm	70°		

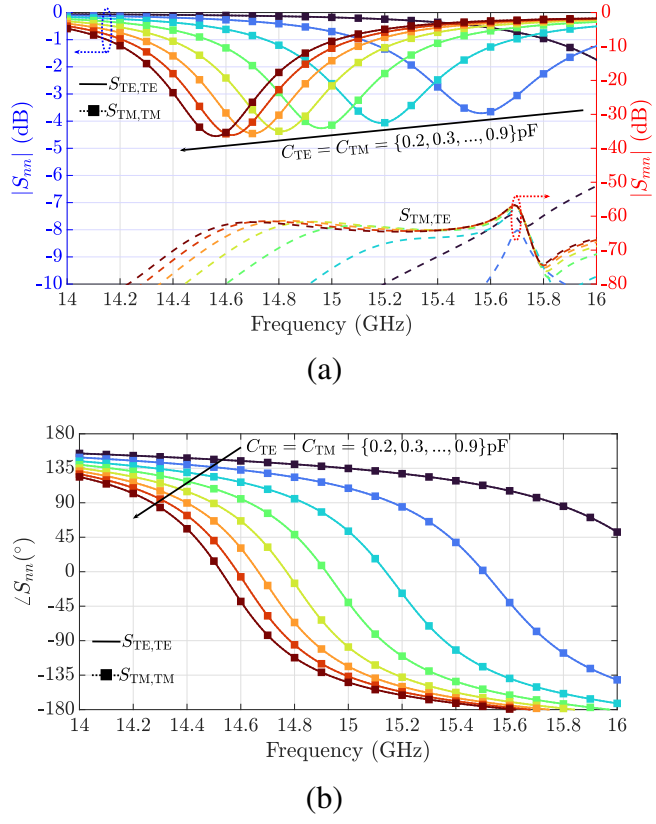


Figure 2. Reflection coefficient of the unit cell: (a) magnitude and (b) phase.

oriented bow-tie (along the y-axis), while the TM mode excites the horizontally oriented bow-tie (along the x-axis). Furthermore, periodic boundary conditions were applied to the side walls of the air box to satisfy the periodicity of the infinite array. A MACOM® MAVR-000120-14110P varactor diode was selected as the phase-tuning component and modeled using a lumped RLC boundary condition. The varactor's equivalent circuit parameters and physical dimensions were obtained from the manufacturer's datasheet.

Figure 2(a) shows the magnitude of the unit cell's reflection coefficient under broadside illumination for various varactor capacitance values ranging from 0.2 to 0.9 pF in 0.1 pF increments. The left y-axis represents the co-polarized reflection (i.e., the incident and reflected modes are the same, $S_{TE,TE}$ or $S_{TM,TM}$), whereas the right y-axis corresponds to the cross-polarized reflection (i.e., the incident and reflected modes are orthogonal, $S_{TM,TE}$). It can be observed that the reflection loss is approximately 4.5 dB within the 14–16 GHz band, while the XPI exceeds 55 dB. Similarly, Fig. 2(b) illustrates the co-polarized reflection phase for the same capacitance range. A phase shift of 270° is achieved within the 14.8–15.2 GHz band, enabling the use of a 2-bit phase resolution to quantize the desired RIS phase distribution. The bandwidth is even larger for a 1-bit phase resolution (i.e., a 180° phase difference), reaching approximately 1.5 GHz. Owing to the varactor diode's continuous tuning capability, a 1-bit phase resolution can be achieved at any frequency within this bandwidth by applying appropriate DC bias voltages. In summary, the 2-bit phase-resolution bandwidth is 400 MHz under far-field illumination, whereas the 1-bit phase-resolution bandwidth extends to 1.5 GHz in near-field RIS deployments, as 1-bit coding suffers from symmetric-beam effects in far-field scenarios [23]. The varactor diode's capacitance range may limit the achievable phase-shift range. A higher capacitance ratio can increase the phase range. On the other hand, reduced substrate thickness can also extend the phase range, but this may introduce a trade-off by increasing

https://doi.org/10.1017/S1759078726103341 Published online by Cambridge University Press

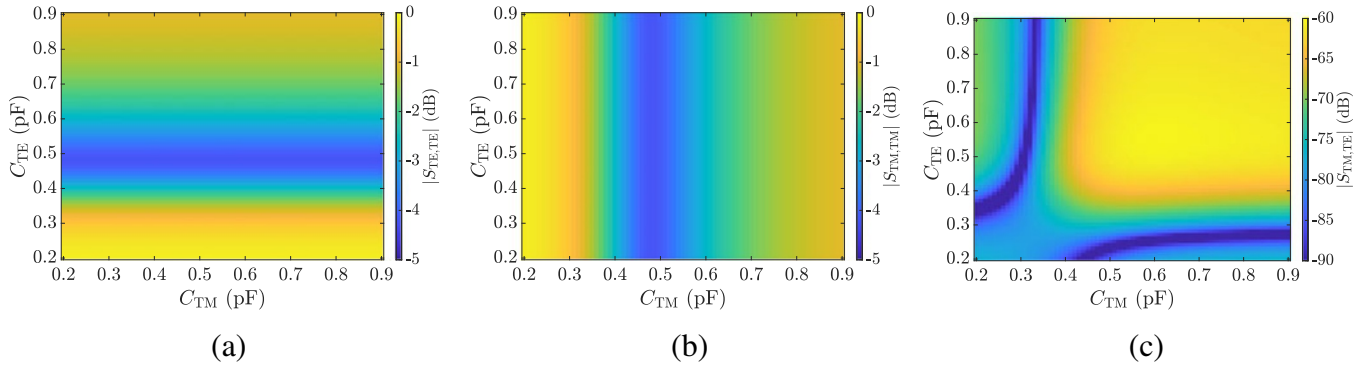


Figure 3. Magnitude of the unit cell's reflection coefficient for various capacitance combinations of the vertical and horizontal varactor diodes at 15 GHz: (a) TE/TE, (b) TM/TM, and (c) TM/TE.

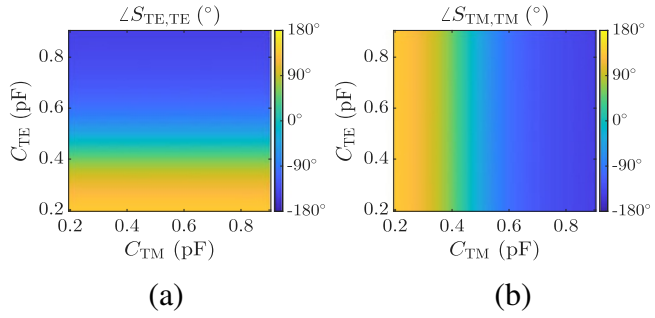


Figure 4. Phase of the unit cell's reflection coefficient for various capacitance combinations of the vertical and horizontal varactor diodes at 15 GHz: (a) TE/TE and (b) TM/TM.

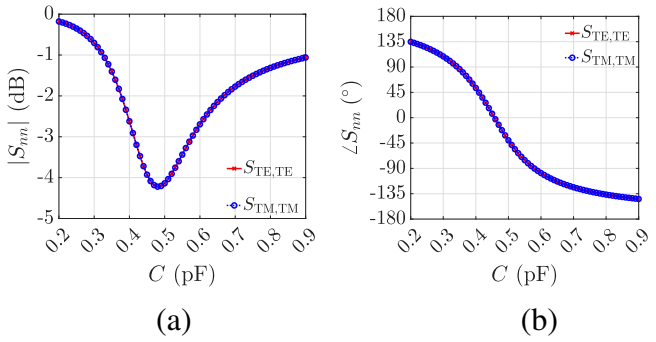


Figure 5. Reflection coefficient of the unit cell at 15 GHz: (a) magnitude and (b) phase.

phase slope, reducing bandwidth, and increasing reflection loss. Therefore, the proposed unit cell is designed to balance this trade-off.

Figure 3(a) and (b) shows the $|S_{\mathrm{TE,TE}}|$ and $|S_{\mathrm{TM,TM}}|$ responses of the unit cell for various capacitance combinations of the vertical and horizontal varactor diodes at the center frequency of 15 GHz, respectively. The maximum reflection loss is approximately 4.2 dB. On the other hand, XPI is more than 61 dB for all capacitance combinations as illustrated in Fig. 3(c). Similarly, Fig. 4(a) and (b) shows the phase of the co-polarized reflection coefficients. The maximum phase shift range achieved is around 279°. It can be observed that both polarizations can be controlled independently. In other words, when the capacitance of one varactor diode is varied while the other is kept fixed, only the corresponding polarization's reflection coefficient changes, whereas the other polarization remains unaffected. Figure 5 illustrates the diagonal of the capacitance-combination matrices. It can be seen that the unit cell exhibits the same behavior for both polarizations, which is also consistent with the observations in Fig. 2.

Figure 6(a) illustrates the magnitude of the surface current distribution on the radiating elements under TE-polarized broadside illumination. The bow-tie element, which integrates the varactor-diode function, serves as the main resonator and enables polarization-dependent tuning. It is observed that only the vertically polarized bow-tie element resonates, whereas the horizontally polarized one remains non-resonant. Under TM-polarized illumination, however, the horizontally oriented bow-tie element becomes resonant while the other does not, as shown in Fig. 6(b). This behavior enables independent control for each polarization. The square ring and patch elements, being dual-polarized, resonate under both polarization states. Similarly, Fig. 6(c) and (d) shows the magnitude of the surface current distribution on the radial stub and the transmission lines – which route the DC bias voltages to the varactor diodes through via holes – under TE- and TM-polarized illumination, respectively. It is observed that the RF power does not propagate through the radial stub, thereby protecting the DC bias network.

Figure 7 shows the normalized radiation pattern of the unit cell in the E-plane (xz-plane, Fig. 7(a)) and H-plane (yz-plane, Fig. 7(b)) under TE- and TM-polarized normal incidence at 15 GHz. The results indicate that the unit cell exhibits a hemispherical radiation pattern. Because the unit-cell analysis employs periodic boundary conditions together with a Floquet port excitation, the array is assumed to be infinite; therefore, no edge diffraction occurs. Consequently, no back radiation is observed. Additionally, the half-power beamwidth of the unit cell is approximately 86.5°, providing a wide beam-steering capability.

RIS design and simulation

Figure 8(a) shows the array (RIS) configuration of the proposed unit cell. Since there are two varactor diodes per cell, we require two capacitances or phase distributions (one for TE, one for TM polarization) to steer the corresponding beam in the desired direction. Let us assume that there are M rows and N columns in the

https://doi.org/10.1017/S1759078726103341 Published online by Cambridge University Press

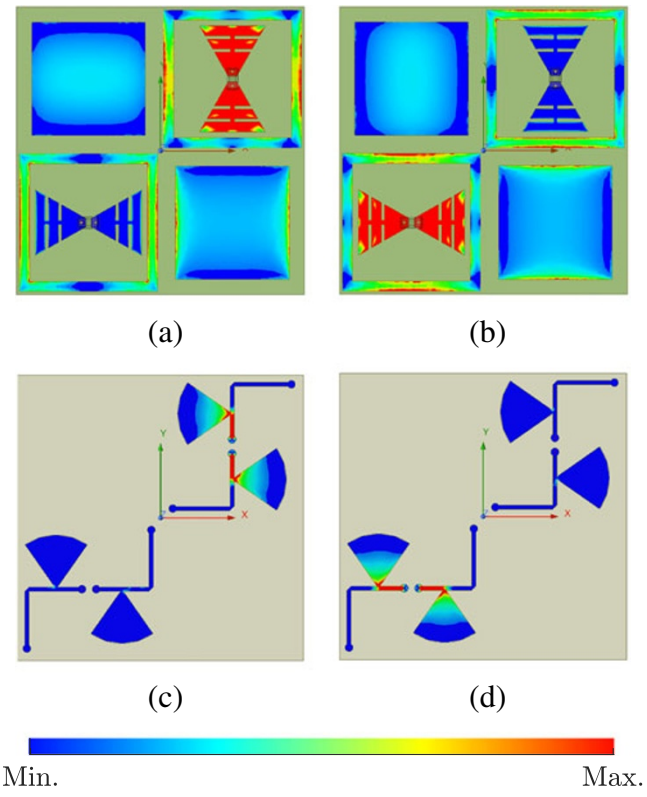


Figure 6. Surface current density magnitude at 15 GHz for $C_{\mathrm{TE}} = C_{\mathrm{TM}} = 0.46$ pF: radiation elements under (a) TE and (b) TM polarization, and radial stubs with transmission lines under (c) TE- and (d) TM-polarized broadside illumination.

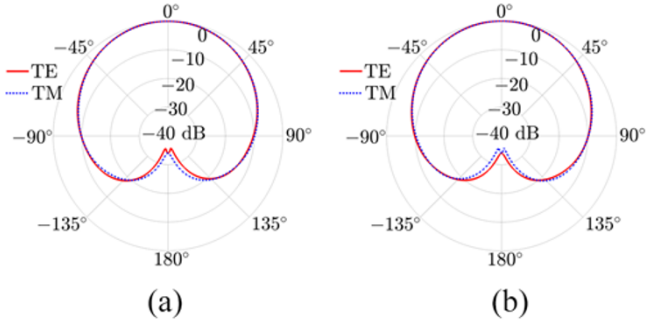


Figure 7. Normalized radiation pattern of the unit cell at 15 GHz: (a) E-plane and (b) H-plane.

RIS. The array factor of a planar antenna array is given as [24]:

$$\mathrm{AF}_p(\theta, \phi) = \sum_{m=1}^{M} \sum_{n=1}^{N} I_{mn,p} e^{j\mathbf{k}\cdot\mathbf{r}_{mn}}, \tag{1}$$

where I is the weight set of the array and $p = \{\mathrm{TE}, \mathrm{TM}\}$ indicates the polarization state. In the case of RIS, the elements' weights can be expressed as:

$$I_{mn,p} = |I_{mn,p}| e^{j\psi^{\mathrm{ppd}}_{mn,p}} = |\Gamma_{mn,p}| e^{j\psi^{\mathrm{r}}_{mn,p}} e^{j\psi^{\mathrm{spd}}_{mn,p}}, \tag{2}$$

where $\Gamma_{mn,p} = |\Gamma_{mn,p}| e^{j\psi^{\mathrm{r}}_{mn,p}}$ is the reflection coefficient of the associated cell, $\psi^{\mathrm{ppd}}_{mn,p} = -\mathbf{k}_{\mathrm{r},p} \cdot \mathbf{r}_{mn}$ is the required progressive phase delay between the cells to steer the beam in a desired direction $(\theta_{\mathrm{r},p}, \phi_{\mathrm{r},p})$, and $\psi^{\mathrm{spd}}_{mn,p} = -\mathbf{k}_{\mathrm{i},p} \cdot \mathbf{r}_{mn}$ is the spatial phase delay created by the incident wave $(\theta_{\mathrm{i},p}, \phi_{\mathrm{i},p})$ due to the different positions of the cells. The only unknown is the reflection phase of each element. Thus, it can be found as:

$$\psi^{\mathrm{r}}_{mn,p} = \psi^{\mathrm{ppd}}_{mn,p} - \psi^{\mathrm{spd}}_{mn,p}. \tag{3}$$

The progressive and spatial phase delays are

$$\psi^{\mathrm{ppd}}_{mn,p} = -k(x_{mn} \sin\theta_{\mathrm{r},p} \cos\phi_{\mathrm{r},p} + y_{mn} \sin\theta_{\mathrm{r},p} \sin\phi_{\mathrm{r},p}), \tag{4a}$$

$$\psi^{\mathrm{spd}}_{mn,p} = k(x_{mn} \sin\theta_{\mathrm{i},p} \cos\phi_{\mathrm{i},p} + y_{mn} \sin\theta_{\mathrm{i},p} \sin\phi_{\mathrm{i},p}), \tag{4b}$$

where k is the wavenumber in air, and (x_{mn}, y_{mn}) are the Cartesian coordinates of the $(m, n)^{\mathrm{th}}$ cell on the RIS surface plane.

As an example, the proposed dual-polarized unit cell was used to construct a 16×16 RIS panel ($M = N = 16$). The RIS was illuminated by an incident plane wave from the broadside ($\theta_{\mathrm{i},p} = 0°$, $\phi_{\mathrm{i},p} = 0°$), as shown in Fig. 8(b). The reflection angles of both polarizations were assumed to be identical ($\theta_{\mathrm{r,TE}} = \theta_{\mathrm{r,TM}}$) and were swept from $-60°$ to $60°$ in $15°$ increments. The corresponding phase distributions were obtained from (3) and (4). The resulting phase delays were continuous. Due to the continuous tuning capability of the varactor diodes, these values could be used within the available phase range of 279° at 15 GHz. However, a 2-bit phase resolution was employed for simplicity in simulation. Four capacitance states were selected from Fig. 5(b) as #[0, 1, 2, 3] = [0.74, 0.485, 0.396, 0.2] pF, providing four distinct phase states [−135°, −45°, 45°, 135°], respectively.

Figure 9 shows the simulated radar cross section (RCS) of the RIS for the considered scenarios. The colors in the plots represent different reflection angles; solid lines indicate the RCS under TE-polarized illumination, while dotted lines represent the RCS under TM-polarized incidence. Figure 9(a) illustrates the co-polarized RCS components for both TE and TM polarization, with the radiation pattern of the unit cell included as a dashed line to highlight the tapering effect of the element pattern on the array factor. This curve does not represent the peak RCS level; instead, it serves as an envelope that indicates the influence of the element pattern on the RIS response across different reflection angles. The unit-cell radiation pattern is obtained from the simulations and was previously presented in Fig. 7. On the other hand, Fig. 9(b) shows the cross-polarized components. The results indicate that the RIS provides accurate wide-angle beam-steering capability within ±60°, with maximum beam-pointing errors of 1.7° and 1.2° for TE and TM polarization, respectively. The RCS values for TE- and TM-polarized illumination are nearly identical within the ±45° beam-steering range, where the beam-pointing error remains below 1°. The peak RCS points follow the radiation pattern of the unit cell except at ±15°, where larger 2-bit quantization errors result in stronger side-lobes. Moreover, the peak RCS under TM polarization is approximately 1.2 dB higher than that under TE polarization at ±60°, which may be attributed to the non-symmetric geometry of the RIS panel. Examining the cross-polarized components, the cross-polarization discrimination (XPD) exceeds 45 dB at 15 GHz. The capacitance distribution of the diodes for each scenario is provided in Table 2.

Figure 10 illustrates the RIS array-factor (1) performance for different phase-resolution techniques. It is observed that, with 2-bit phase resolution, the quantization loss – defined as the difference in dB between the peak values of the continuous and quantized array factors – is approximately 1 dB. When a quasi-continuous phase distribution is employed – i.e., continuous within the achievable phase-shift range and mapped to the nearest boundary outside this

https://doi.org/10.1017/S1759078726103341 Published online by Cambridge University Press

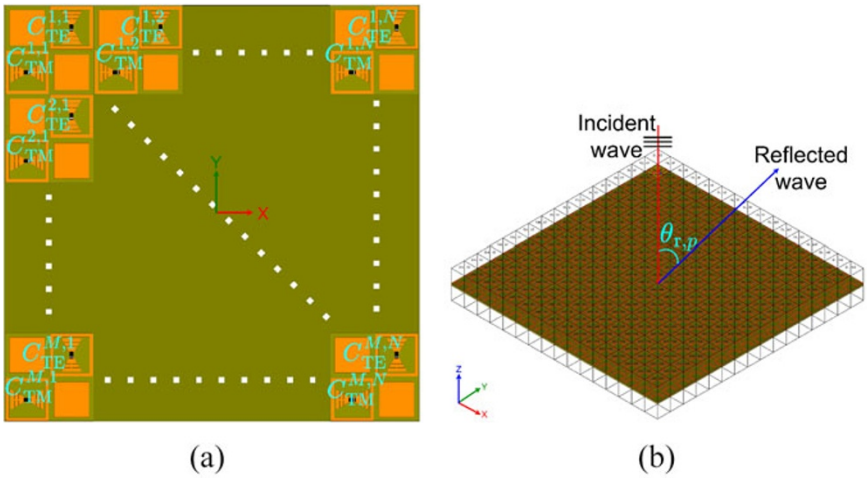


Figure 8. RIS (a) topology and (b) view of 16×16 panel.

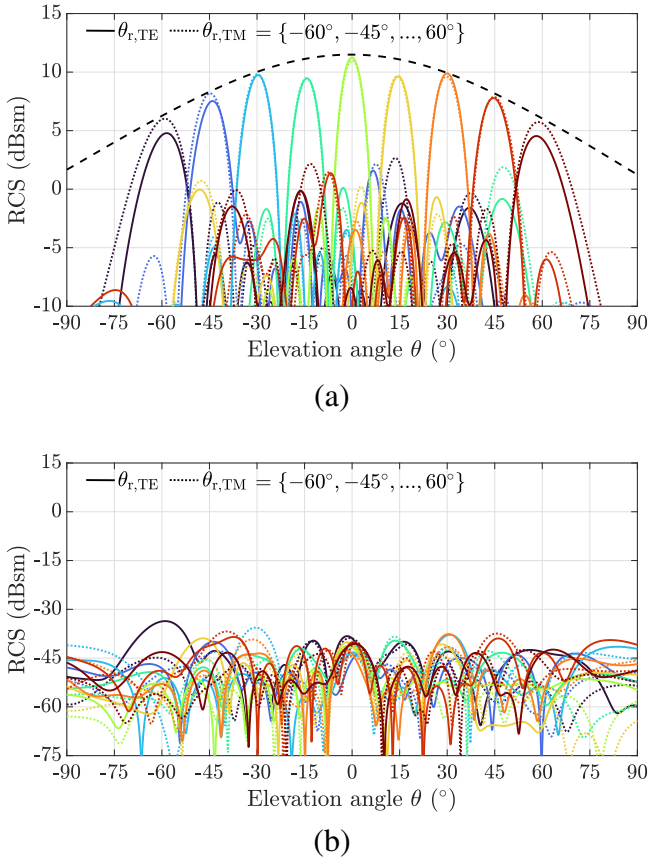


Figure 9. Simulated RCS of the RIS for various reflection angles under broadside plane-wave incidence at 15 GHz: (a) co-polarized RCS components, with the unit cell radiation pattern shown as a dashed line, and (b) cross-polarized RCS components.

Table 2. RIS capacitance distributions for various reflection angles under broadside plane-wave illumination at 15 GHz

Reflection angle ($\theta_{r,p}$)	Configuration
0°	0000000000000000
−15° / 15°	2233001122330011 / 1100332211003322
−30° / 30°	2031023012030123 / 1032103210321032
−45° / 45°	3032131201202130 / 0310210213213203
−60° / 60°	1202313102021312 / 2131020213132021

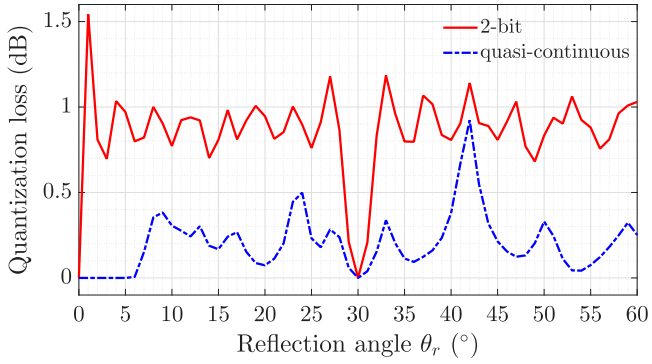


Figure 10. RIS array factor performance under normal incidence with different phase resolution techniques.

range – the quantization loss is reduced to below 0.5 dB. This technique is advantageous because the capacitance of varactor diodes can be continuously controlled via the applied reverse-bias voltage. Furthermore, at 30° (corresponding to a 90° phase shift between adjacent columns), the quantized and continuous phase distributions coincide, resulting in no quantization loss. Since there is no quantization error at 0° and ±30°, the RCS at ±15° is lower than the RCS values at those angles.

To illustrate the independent control of both polarizations and the beam-steering performance within the 2-bit phase resolution bandwidth (i.e., 14.8–15.2 GHz), vertically placed varactor diodes were configured for $\theta_{r,TE} = 30°$, while horizontally placed varactor diodes were configured for $\theta_{r,TM} = -30°$, with the angle of incidence set to broadside. As shown in Fig. 11, the reflected beam from the RIS is directed toward −30° under a TM-polarized incident plane wave and toward 30° under a TE-polarized incident wave at 14.8, 15, and 15.2 GHz. The beam-pointing error remains below 1°; however, the specular reflection increases because the phase distribution on the RIS surface is not ideally matched, resulting in reduced beam-steering performance, similar to a beam-squint effect.

https://doi.org/10.1017/S1759078726103341 Published online by Cambridge University Press

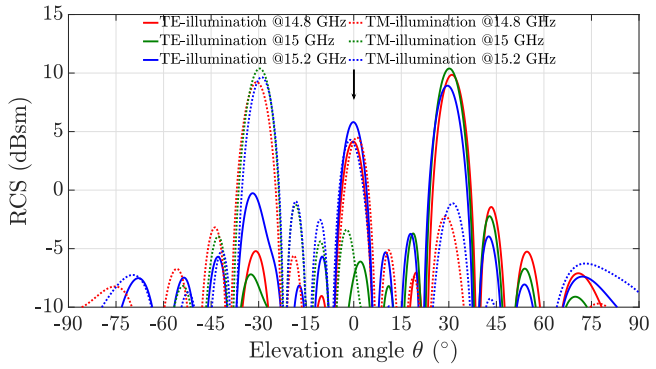


Figure 11. Simulated RCS of the RIS under broadside plane-wave illumination with $\theta_{r,TM} = -30^\circ$ and $\theta_{r,TE} = 30^\circ$ at different frequency points.

Figure 12(a) shows the RCS of the RIS under oblique incidence. The angles of incidence for the TE- and TM-polarized plane waves were set to $\theta_{i,TE} = 60^\circ$ and $\theta_{i,TM} = -60^\circ$, respectively, while the reflected beams were configured for $\theta_{r,TE} = \theta_{r,TM} = 0^\circ$. Due to the angular reciprocity of the RIS, the same capacitance configurations listed in Table 2 could be used. It is observed that under wide oblique incidence, beam steering remains highly accurate, with an error below 0.5°. The difference between the anomalous reflection (steered beam) and the specular reflection under TE-polarized illumination is approximately 10.8 dB, whereas it is reduced under TM-polarized illumination, despite the higher peak RCS. This behavior may be attributed to the fact that the unit cell responds differently under wide oblique incidence for the two polarizations. The capacitance states do not maintain the required 90° phase spacing under wide oblique incidence, leading to increased quantization error. To demonstrate the angular robustness of the proposed RIS, the array was evaluated under different incidence and reflection scenarios. Figure 12(b) shows the RCS in the $\phi = 0^\circ$ plane when the RIS is configured for $\theta_{i,TM} = 25^\circ$, $\theta_{i,TE} = -40^\circ$, $\theta_{r,TM} = -15^\circ$, and $\theta_{r,TE} = 10^\circ$. Similarly, Fig. 12(c) presents the 3D RCS when beam steering is applied in both planes, with $(\theta_{i,p}, \phi_{i,p}) = (-20^\circ, 0^\circ)$ and $(\theta_{r,p}, \phi_{r,p}) = (35^\circ, 45^\circ)$, represented in the u–v domain, where $u \triangleq \sin\theta\cos\phi$ and $v \triangleq \sin\theta\sin\phi$. It is observed that the RIS successfully steers the beam in both planes with low beam-pointing error, even with 2-bit phase resolution.

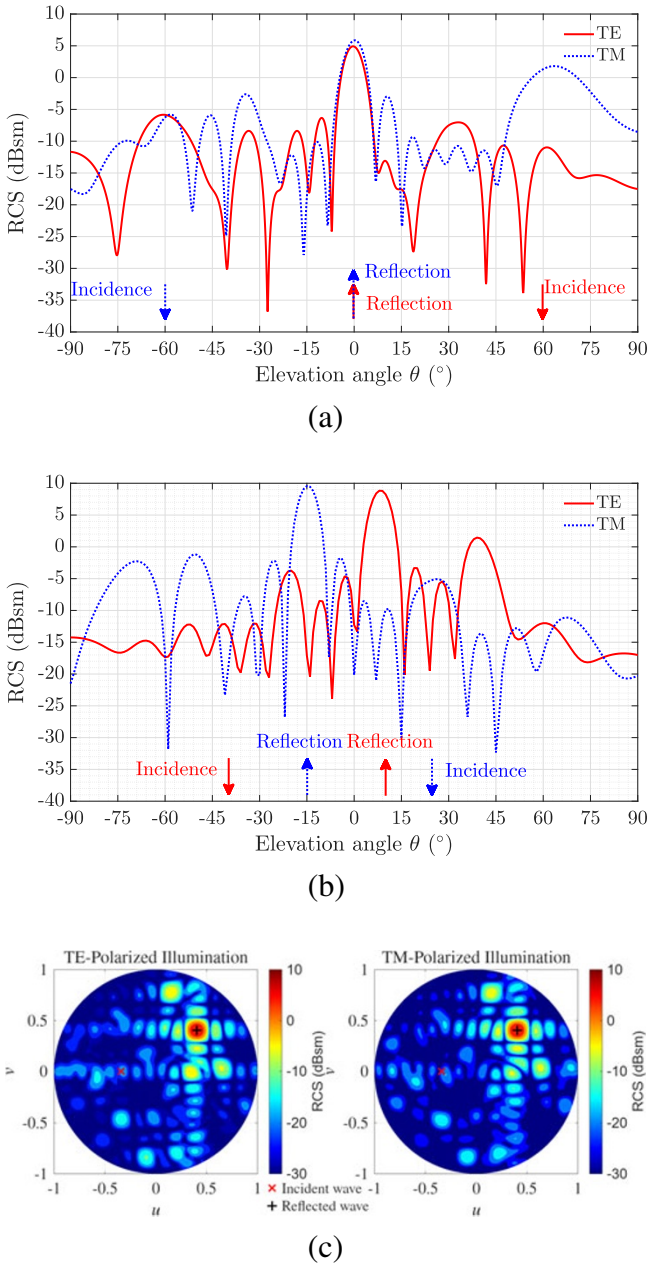


Figure 12. Simulated RCS of the RIS at 15 GHz under oblique incidence. (a) Incident TM: $(-60^\circ, 0^\circ)$, TE: $(60^\circ, 0^\circ)$, reflection: $(0^\circ, 0^\circ)$. (b) TM: incidence $(25^\circ, 0^\circ)$, reflection $(-15^\circ, 0^\circ)$; TE: incidence $(-40^\circ, 0^\circ)$, reflection $(10^\circ, 0^\circ)$. (c) TM, TE: incidence $(-20^\circ, 0^\circ)$, reflection $(35^\circ, 45^\circ)$.

Experimental validation of the unit cell

There are several methods to validate the characteristics of a unit cell. One common approach is to use a waveguide simulator [25], in which the unit cell is inserted into a waveguide to measure the phase and magnitude of the reflected waves. However, this technique does not account for the coupling between adjacent cells. In other words, the periodic boundary conditions typically employed in full-wave simulations are not replicated in this measurement setup. As a result, mutual coupling effects between unit cells are not considered. Two unit cells may also be inserted into a waveguide to partially account for mutual coupling, although only the coupling from one neighboring side is captured [10]. Another approach is to measure the macroscopic response of the entire surface, which can be used to validate the unit cell's characteristics [26]. To incorporate coupling from all surrounding elements, the unit cell can be characterized by placing it at the center of a 3 × 3 array [6]. The 3 × 3 array constitutes the minimum configuration that approximates the mutual coupling in periodic boundary conditions. In this setup, the central element is coupled to all surrounding elements, whereas the edge elements are only partially coupled. Nevertheless, this configuration provides a reasonable representation of the electromagnetic environment in simulation using a minimum number of elements. Figure 13(a) shows the fabricated 3 × 3 prototype of the proposed unit cell. To bias the varactor diodes, DC pin headers were placed on the backside of the prototype, and these pins were connected to the corresponding via holes through DC traces, as illustrated in Fig. 13(b). To further minimize RF leakage, thick film 10 kΩ resistors were included in the biasing network. Figure 13(c) shows the schematic of the bias circuit. The anodes of all varactor diodes are connected to ground, while their cathodes are connected

https://doi.org/10.1017/S1759078726103341 Published online by Cambridge University Press

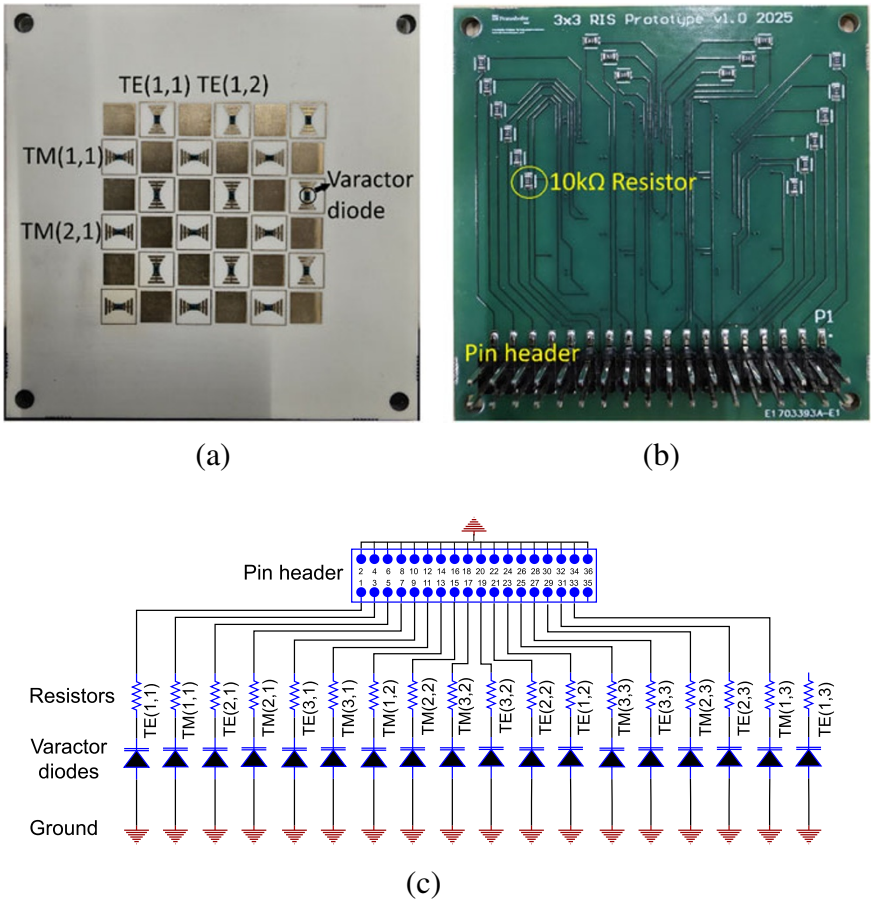


Figure 13. Fabricated 3×3 prototype: (a) top view with varactor diode IDs, (b) bottom view, and (c) schematic of the biasing circuit.

to the input-voltage pins through resistors. Since all varactor diodes are reverse-biased, no DC current flows through the resistors, and therefore no DC voltage drop occurs across them.

Monostatic measurement

Figure 14(a) shows the monostatic measurement setup used for the fabricated prototype. An R&S®HMP2030 power supply (PS) was used to bias the varactor diodes. The first channel of the PS was assigned to the vertically oriented varactor diodes, while the second channel was assigned to the horizontally oriented ones. Half of the top DC bias pins on the prototype were connected to the first channel, and the remaining pins were connected to the second channel. The bottom pins were connected to ground. An MVG QH2000 open-boundary quad-ridge horn antenna was used as the measurement antenna, and its ports were connected to an R&S®ZVA24 vector network analyzer (VNA). The separation between the measurement antenna and the prototype was set to 35 cm. To enable remote control, a controller PC was connected to both the VNA and the PS through an Ethernet switch. Absorber walls were placed behind the prototype and in front of the PS and VNA to reduce reflections from the equipment and the surrounding environment. The measurement environment is shown in Fig. 14(b).

The VNA was calibrated using an R&S®ZV-Z52 electronic calibration kit to compensate for systematic errors introduced by the cables and connectors. The reflection coefficients of the measurement antenna (i.e., S_{11}, S_{22}) were then measured under different reverse-bias voltages applied to the varactors, ranging from 0 to 10 V. Measurements taken with the prototype were divided by the antenna-only measurement (without the prototype) to obtain the reflection magnitude associated with the RIS. Although absorber walls were used, the measurement environment still introduced multipath reflections; therefore, time-gating was applied to the collected data.

Figure 15 shows the measured normalized reflection coefficient magnitude at 15 GHz for various reverse-bias voltages. Note that all varactor diodes were biased with the same voltage. The resulting reflection-magnitude trend resembles that obtained in the simulation, with a slight shift. This shift is most likely attributed to fabrication tolerances, which can cause a frequency shift in the response. The difference observed between the two polarization states may be attributed to the nonidentical responses of the two antenna ports. The maximum reflection loss of the prototype is approximately 7 dB, which is slightly higher than that observed in the simulations. This discrepancy may be attributed to the internal resistance of the varactor diodes, which might be slightly higher than the values used in the simulation model. Furthermore, the elements in the 3×3 array do not exhibit identical electrical behavior. While the central element is affected by mutual coupling from all surrounding elements, the edge elements experience reduced coupling. Consequently, even when identical bias voltages are applied, the response of each unit cell may differ. This non-uniformity can disturb the intended phase distribution across the surface and distort the reflected beam. As a result, a portion of the reflected power may be redirected into side lobes, appearing as a loss at the receiver,

https://doi.org/10.1017/S1759078726103341 Published online by Cambridge University Press

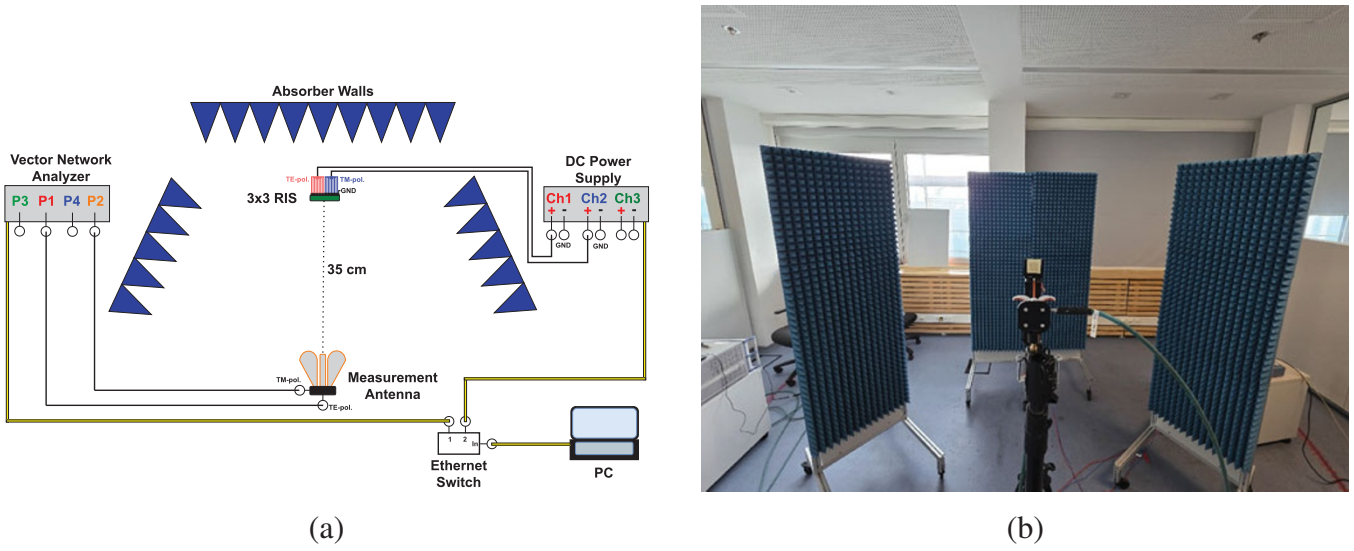


Figure 14. Monostatic measurement setup: (a) block diagram and (b) photograph of the environment.

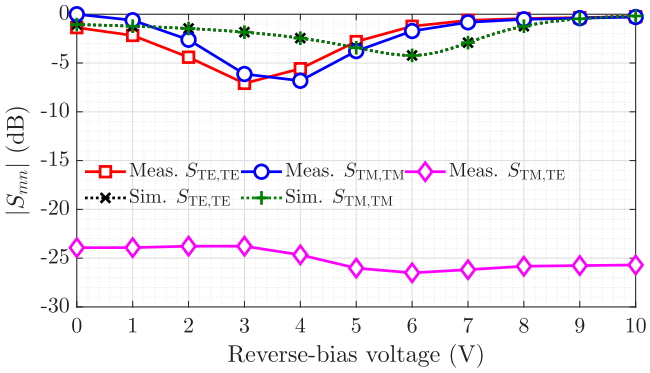


Figure 15. Monostatic measurement of the reflection magnitude for various reverse-bias voltages at 15 GHz.

although it does not correspond to true absorptive loss. The reflection loss can be reduced by increasing the substrate thickness, but this comes at the expense of a narrower phase-shift range.

There is a certain deterioration in the measured XPI relative to the simulated one. This discrepancy may arise from several factors. First, the excitation used in simulations is an ideal plane-wave source, whereas in measurements, the antenna cannot perfectly generate a linearly polarized plane wave over the prototype surface. Moreover, a dual-polarized antenna is employed as the measurement antenna, and its port-to-port isolation is not perfect, which can further degrade the XPI. In addition, the prototype is very small, making precise alignment between the antenna and the unit cell challenging. Not only must the direct alignment be accurate, but the dual-polarized measurement antenna must also be oriented exactly at 90°. Even a slight rotation of the measurement antenna or a small misalignment between the antenna and the prototype may increase polarization leakage. Although time-gating was applied, residual reflections from the surrounding environment may still contribute to deterioration – for example, reflections from the tripod positioned at the same distance as the prototype – since the measurement environment is not fully anechoic. Finally, due to the small size of the varactor diodes, they cannot be positioned with perfect accuracy during soldering, leading to placement errors. These placement errors and potential damage to varactor diodes may result in non-ideal biasing. Despite these factors, the measured XPI values, although lower than the simulated ones, remain around 24 dB.

Bistatic measurement

Although variations in the reflection magnitude of the prototype were observed for different bias voltages, corresponding variations in the phase response could not be clearly identified in the monostatic measurements. This may be because the phase response of the antenna port dominates the overall reflection phase, masking the contribution from the prototype, since the prototype is very small and the backscatter is very weak. Therefore, a bistatic measurement setup was employed, as shown in Fig. 16(a), to estimate the reflection phase of the prototype more accurately. Two MVG QH2000 open-boundary quad-ridge horn antennas were used as the transmit (Tx) and receive (Rx) antennas, each oriented toward the prototype at 10°. The distance between the antennas and the prototype was set to 185 cm to reduce direct interaction between the Tx and Rx antennas. All other measurement equipment remained the same, and the bistatic measurement environment is presented in Fig. 16(b).

In this configuration, the transmission coefficient was measured using the VNA for different reverse-bias voltages applied to the varactors, ranging from 0 to 10 V. Due to the non-anechoic environment, time-gating was applied to all measurements. The prototype was then replaced with a metal plate of similar size, and the measurement was repeated with the same time-gating parameters. As a post-processing calibration step, the measurements obtained with the prototype were divided by the corresponding metal-plate measurements. Figure 17 shows the measured reflection coefficient phase at 15 GHz for various reverse-bias voltages. It is observed that the maximum phase shift is approximately 270°, and the curves are similar to those obtained from simulations, exhibiting a shift comparable to that observed in the monostatic measurements.

Due to its small size and the relatively large distance between the antennas and the prototype, the magnitude of the reflected

https://doi.org/10.1017/S1759078726103341 Published online by Cambridge University Press

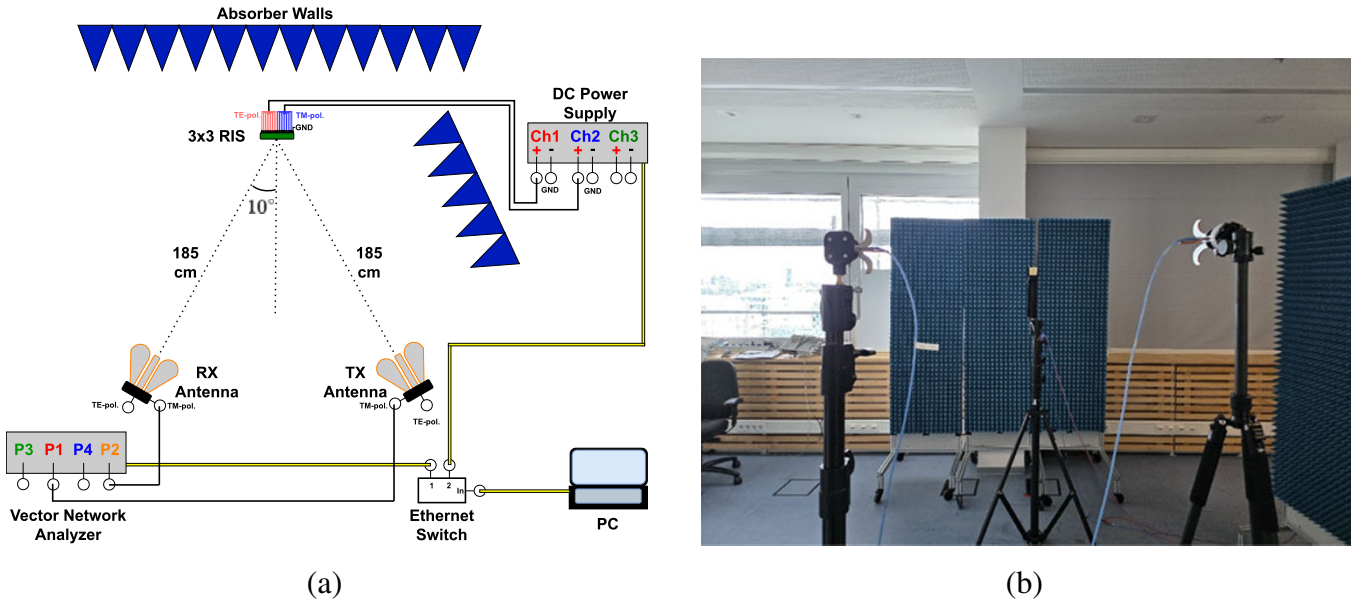


Figure 16. Bistatic measurement setup: (a) block diagram and (b) photograph of the environment.

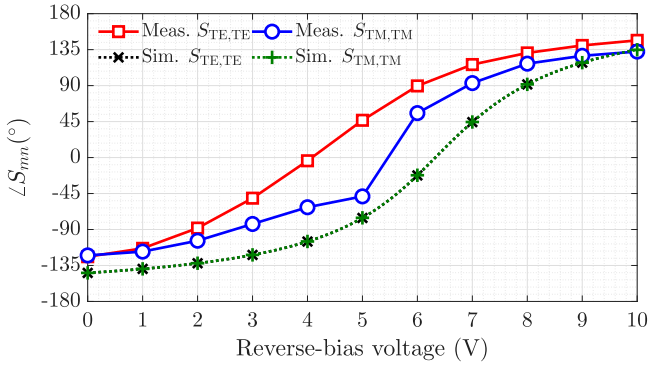


Figure 17. Bistatic measurement of the reflection phase for various reverse-bias voltages at 15 GHz.

wave from the RIS is very weak, and the variations in magnitude are not as pronounced as in the monostatic case. This indicates that, for small surfaces, bistatic setups are more suitable for phase measurements, whereas monostatic setups are more appropriate for magnitude measurements. For larger surfaces, however, both measurement techniques are expected to provide similar results.

The total efficiency of the RIS can be defined as the ratio between the measured and ideal values for bistatic scenarios – without accounting for measurement tolerances [27]:

$$\eta_{\text{tot}} := \frac{\left|S_{21}^{\text{meas}}(\theta_{\text{r}})\right|^2}{\left|S_{21}^{\text{ideal}}(\theta_{\text{i}}, \theta_{\text{r}})\right|^2}. \tag{5}$$

The ideal forward transmission (S-parameter) coefficient can be found from the bistatic radar equation:

$$\left|S_{21}^{\text{ideal}}(\theta_{\text{i}}, \theta_{\text{r}})\right|^2 = \sigma(\theta_{\text{i}}, \theta_{\text{r}}) \frac{G^2}{4\pi} \left(\frac{\lambda}{4\pi R^2}\right)^2, \tag{6}$$

assuming that both the Tx and Rx antennas have the same realized gain (G) and are located at the same distance (R) from the RIS, the RCS of the RIS in an ideal case is given by [28]

$$\sigma(\theta_{\text{i}}, \theta_{\text{r}}) = 4\pi \frac{(L_x L_y)^2}{\lambda^2} \cos\theta_{\text{i}} \cos\theta_{\text{r}}, \tag{7}$$

where (L_x, L_y) is the size of the RIS.

When all the diodes are biased with the same voltages, only the specular reflection occurs and $\theta_{\text{i}} = \theta_{\text{r}}$. From the bistatic unit-cell measurements, the total efficiency of the RIS prototype was found to be approximately 42% under a reverse zero-voltage bias.

To validate the unit cell's radiation performance, a bistatic radiation pattern measurement setup was implemented. Figure 18(a) shows the diagram of the measurement setup. The 3×3 RIS prototype was mounted at the center of a rotating stage (rotary gimbal), and the TX antenna was positioned 50 cm away from the prototype, pointing towards it, using a carbon pipe. Therefore, the prototype and Tx antenna rotate together, and the angle of incidence is always from boresight. The Rx antenna was placed 125 cm away from the prototype, and its position was fixed. All the diodes were biased at 0 V, and the measurements were performed using the VNA. Measurements were recorded at each angular position of the gimbal, ranging from -90° to 90° with 1° increments. Figure 18(b) shows the measurement environment.

Figure 19 depicts the normalized radiation pattern of the prototype. Ideally, the unit-cell radiation pattern could be extracted using theoretical array-factor calculation. However, since not all cells behave identically due to mutual-coupling effects, a full-wave simulation of a 3×3 array was performed and is provided alongside the measurements for comparison. Due to the non-anechoic measurement environment, fluctuations are observed in the measured pattern – despite the utilization of the time-gating technique in post-processing. Furthermore, a blind spot appears around 0°. This is caused by the shadowing/blockage effect of the Tx antenna, which is positioned in front of the Rx antenna. In addition, as the angle approaches 90°, the gimbal arm begins to block the radiation from the prototype. Despite these effects, the overall envelope of the measured data shows good agreement with the simulation results.

https://doi.org/10.1017/S1759078726103341 Published online by Cambridge University Press

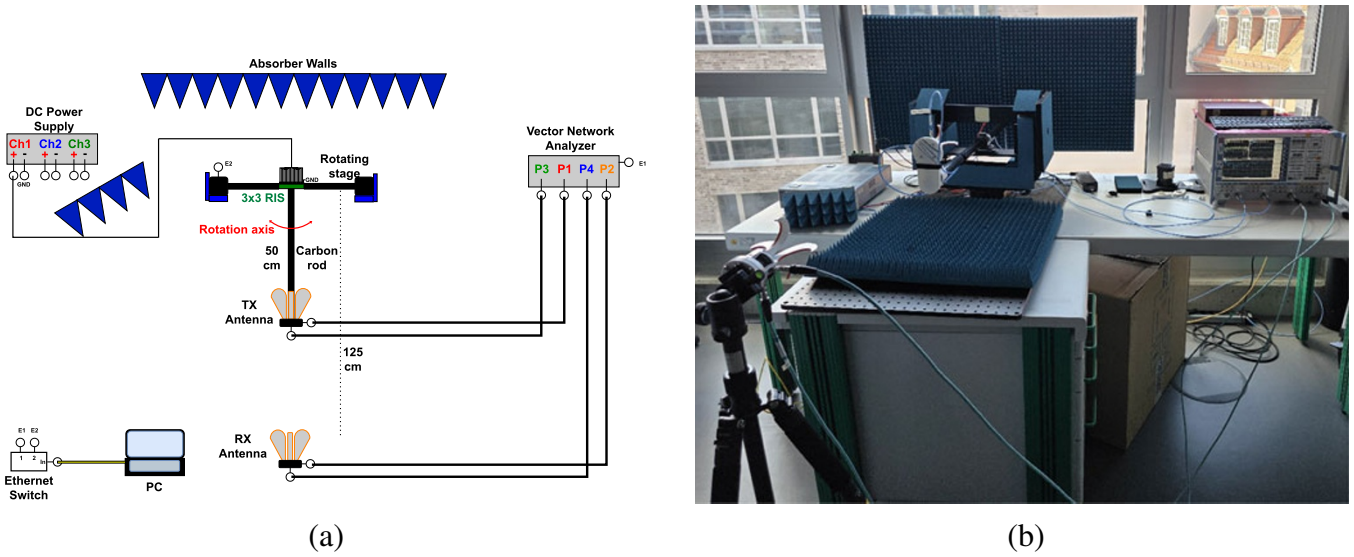


Figure 18. Radiation pattern bistatic measurement setup: (a) block diagram and (b) photograph of the environment.

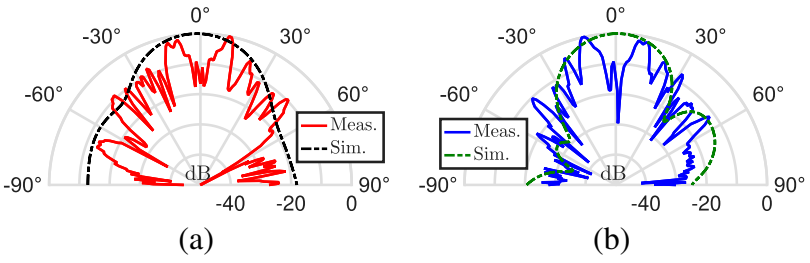


Figure 19. Measured and simulated normalized radiation pattern of 3 × 3 RIS prototype: under (a) TE and (b) TM polarized normal incidence.

Table 3. Comparison of the proposed unit cell with previously reported RIS and reflectarray unit cells

Reference	Polarization	Working frequency	Unit cell size	Tuning component	No. of tuning components	Phase range	Reflection loss	Cross-polarization isolation
[12]	DLP	3.5 GHz	$0.35\lambda_0 \times 0.35\lambda_0$	Varactor diode	2	180°	4.2 dB	20 dB
[9]	DLP	3.5 GHz	$0.35\lambda_0 \times 0.35\lambda_0$	PIN diode	4	270°	2 dB	sim: 61 dB meas: 25 dB
[14]	DLP	4.9 GHz	$0.45\lambda_0 \times 0.45\lambda_0$	Varactor diode	4	370°	3.1 dB	sim: 27 dB meas: 23 dB
[7]	DLP	5.8 GHz	$0.29\lambda_0 \times 0.29\lambda_0$	PIN diode	2	180°	3 dB	10 dB
[13]	CP	11.2 GHz / 15.2 GHz	$0.5\lambda_0^{LB} \times 0.5\lambda_0^{LB}$	Varactor diode	8	300° / > 300°	10 dB / 12 dB	19 dB* / 15 dB*
This Work	DLP	15 GHz	$0.5\lambda_0 \times 0.5\lambda_0$	Varactor diode	2	270°	7 dB	sim: 61 dB meas: 24 dB

Notes: All results presented above are measurement results unless stated otherwise. DLP: dual-linear polarized. CP: circularly-polarized. LB: lower-band. (*) The given values are XPD: cross-polarization discrimination.

Finally, Table 3 provides a comparison between the proposed unit cell and previously reported RIS and reflectarray unit cells. The results show that the proposed unit cell achieves one of the highest XPI levels while providing a phase-shift range of 270° and simultaneously minimizing the number of required tuning components, thus reducing the overall cost of an RIS panel.

Conclusion

A dual-polarized RIS with high XPI operating within the upper mid-band, one of the key candidate spectra for 6G, has been presented. The topology and structure of the proposed unit cell have been discussed, and detailed analyses of both the unit cell and the 16 × 16 RIS have been provided. The number of adjustable

https://doi.org/10.1017/S1759078726103341 Published online by Cambridge University Press

components has been minimized to only two varactor diodes for dual-polarized operation, resulting in lower cost, simpler structure, and improved robustness. Simulation results show that the unit cell achieves more than 270° of phase-shift range with a maximum reflection loss of 4.5 dB and an XPI exceeding 61 dB within the 14.8–15.2 GHz band. The 16 × 16 RIS achieves a wide beam-scanning capability of ±60° with a maximum simulated beam-pointing error of only 1.7°. To validate the unit-cell characteristics, a 3 × 3 prototype was fabricated. Two different measurement techniques were evaluated to characterize such a small prototype in a non-anechoic environment. The measurement results show good agreement with simulations, providing a phase range of 270°, approximately 7 dB reflection loss, and an XPI of around 24 dB. It is also observed that bistatic measurement setups are more suitable for phase characterization, whereas monostatic setups are more appropriate for magnitude measurements of small surfaces. Overall, the proposed unit cell shows good potential for future 6G applications, particularly in full-duplex and ISAC systems, owing to its high polarization isolation.

As future work, a 16 × 16 RIS panel will be fabricated and tested to validate the array-level performance of the proposed RIS and will be deployed in a full-duplex or ISAC scenario for real-world demonstration.

Acknowledgements. The authors would like to thank the Federal Ministry of Research, Technology, and Space (BMFTR) for supporting the xG-RIC project as part of the research program Communication Systems "Souverän. Digital. Vernetzt" (grant number: 16KIS2429K), and for supporting the DE-TW-GLEMORIS project (grant number: 16ME1100), funded under the framework program for Research and Innovation "Microelectronics. Trustworthy and sustainable. For Germany and Europe" – a BMFTR/NSTC joint funding program: Research collaboration in microelectronics between Germany and Taiwan.

Competing interests. The author(s) declare none.

References

1. **Saad W, Bennis M and Chen M** (2020) A vision of 6G wireless systems: Applications, trends, technologies, and open research problems. *IEEE Network* **34**(3), 134–142.
2. **Wu Q and Zhang R** (2019) Intelligent reflecting surface enhanced wireless network via joint active and passive beamforming. *IEEE Transactions on Wireless Communications* **18**(11), 5394–5409.
3. **Tohidi E, Askar R, Utkovski Z and Stańczak S** (2023) Full-duplex operation of ISAC: Self-interference reduction from the lens of IRS *2023 IEEE Globecom Workshops (GC Wkshps)*, Kuala Lumpur, Malaysia, pp. 1880–1885.
4. **Chepuri SP, Shlezinger N, Liu F, Alexandropoulos GC, Buzzi S and Eldar YC** (2023) Integrated sensing and communications with reconfigurable intelligent surfaces: From signal modeling to processing. *IEEE Signal Processing Magazine* **40**(6), 41–62.
5. **Kim H, Yang H, Kim H and Oh J** (2025) Integrated sensing and communication using reconfigurable intelligent surface: Hardware, ray-tracing demonstration, and channel measurement in the 6G mid band *2025 IEEE/MTT-S International Microwave Symposium - IMS 2025*, San Francisco, CA, USA, pp. 303–306.
6. **Neuder R, Liu Y, Dzieia N, Wang D and Jiménez-Sáez A** (2024) Unit cell design for dual-polarized liquid crystal reconfigurable intelligent surface based on defected delay lines *2024 54th European Microwave Conference (EuMC)*, Paris, France, pp. 228–231.
7. **Sangmahamad P, Janpugdee P and Zhao Y** (2023) A metasurface-based electronically reconfigurable and dual-polarized reflectarray antenna for beam-steering applications. *IEEE Access* **11**, 137414–137425.
8. **Yin Y, Deng C, Cao X, Hao Y, Hou Y, Xu H and Sarabandi K** (2024) Design of a 2-bit dual-polarized reconfigurable reflectarray with high aperture efficiency. *IEEE Transactions on Antennas and Propagation* **72**(1), 542–552.
9. **Zhu L, Han J, Li G, Ma X, Xia D, Zheng Z, Liu H and Li L** (2024) Dual linearly polarized 2-bit programmable metasurface with high cross-polarization discrimination. *IEEE Transactions on Antennas and Propagation* **72**(2), 1510–1520.
10. **Scheder A, Fleischmann J, Gröschel P and Vossiek M** (2024) Dual polarized 1-bit reconfigurable reflective unit cell design for intelligent reflective surfaces operating in the 5.8 GHz ISM band *2024 54th European Microwave Conference (EuMC)*, Paris, France, pp. 236–239.
11. **Yang N, Zhong YC, Wang H, Yan J, Jia Y, Liu Z-X, Liu Y and Gong S** (2025) A 2-bit programmable metasurface antenna with simple structure, high-level integration, and wide-angle multipolarization beam scanning. *IEEE Transactions on Antennas and Propagation* **73**(10), 7850–7861.
12. **Rains J, Kazim JUR, Tukmanov A, Zhang L, Abbasi Q and Imran M** (2023) Fully-addressable varactor-based reflecting metasurface with dual-linear polarisation for low power reconfigurable intelligent surfaces *2023 17th European Conference on Antennas and Propagation (EuCAP)*, Florence, Italy, pp. 1–5.
13. **Baladi E, Xu MY, Faria N, Nicholls J and Hum SV** (2021) Dual-band circularly polarized fully reconfigurable reflectarray antenna for satellite applications in the Ku-band. *IEEE Transactions on Antennas and Propagation* **69**(12), 8387–8396.
14. **Liu R, Shi H, Zhang Z, Chen X, Chen J, Yi J and Zhang A** (2025) A dual-polarized reconfigurable intelligent surface with low cross-polarization based on guided-wave inspired structure. *IEEE Transactions on Antennas and Propagation* **73**(8), 6074–6078.
15. **Yurtoglu MA and Askar R** (2025) 3D-printed dual-polarized magneto-electric dipole antenna with wideband high isolation for full-duplex applications *2025 19th European Conference on Antennas and Propagation (EuCAP)* Stockholm, Sweden, pp. 1–5.
16. **Yurtoglu MA, Askar R, Leather LA and Peter M** (2026) 3d-printed dual-polarized magneto-electric dipole antenna with > 50-db wideband isolation for full-duplex and icas applications. *International Journal of Microwave and Wireless Technologies* 1–10.
17. **Yurtoglu MA, Askar R, Wittig S, Schmieder M, Peter M and Keusgen W** (2025) 15 GHz independently controllable dual-polarized 2-bit reconfigurable intelligent surface *2025 55th European Microwave Conference (EuMC)* Utrecht, Netherlands, pp. 502–505. https://doi.org/10.23919/EuMC65286.2025.11235104.
18. **Farashahi M, Seet B-C and Li XJ** (2024) Dual-polarized reconfigurable intelligent surface unit cell with single varactor diode *2024 IEEE International Mediterranean Conference on Communications and Networking (MeditCom)* Madrid, Spain, pp. 447–452.
19. **Ke JC, Dai JY, Chen MZ, Wang L, Zhang C, Tang W, Yang J, Liu W, Li X and Lu Y** (2021) Linear and nonlinear polarization syntheses and their programmable controls based on anisotropic time-domain digital coding metasurface. *Small structures* **2**(1), 2000060.
20. **Oh JH, Jeong J, Park Y and Wi S-H** (2023) A 29 GHz dual-polarized reconfigurable intelligent surface with 2-dimensional wide scanning range *2023 17th European Conference on Antennas and Propagation (EuCAP)* Florence, Italy, pp. 1–5.
21. **Venneri F and Costanzo S** (2025) Dual polarized dual coverage reflectarray-based passive reflecting surface for next-generation networks. *IEEE Open Journal of Antennas and Propagation* **6**(6), 2050–2061.
22. **Tolin E and Bahr A** (2024) Phase stable 2-bit reconfigurable reflective metasurface for 6G wireless communications *2024 IEEE International Symposium on Antennas and Propagation and INC/USNC-URSI Radio Science Meeting (AP-S/INC-USNC-URSI)* Firenze, Italy, pp. 1183–1184.
23. **Da Silva LG, Chu Z, Xiao P and Cerqueira AS** (2023) A varactor-based 1024-element ris design for mm-waves. *Frontiers in Communications and networks*, **4** 1086011.
24. **Balanis CA** (2016) *Antenna Theory: Analysis and Design.* Hoboken, New Jersey, USA.: John wiley & sons.

25. **Abbasi MI and Ismail MY** (2011) Reflection loss and bandwidth performance of X-band infinite reflectarrays: Simulations and measurements. *Microwave and Optical Technology Letters* **53**(1), 77–80, https://onlinelibrary.wiley.com/doi/abs/10.1002/mop.25662.
26. **Araghi A, Khalily M, Safaei M, Bagheri A, Singh V, Wang F and Tafazolli R** (2022) Reconfigurable intelligent surface (RIS) in the sub-6 GHz band: Design, implementation, and real-world demonstration. *IEEE Access* **10** 2646–2655.
27. **Ataloglou VG and Eleftheriades GV** (2025) A reconfigurable intelligent surface with surface-wave assisted beamforming capabilities. *IEEE Transactions on Antennas and Propagation* **73**(8), 5346–5359.
28. **Trichopoulos GC, Theofanopoulos P, Kashyap B, Shekhawat A, Modi A, Osman T, Kumar S, Sengar A, Chang A and Alkhateeb A** (2022) Design and evaluation of reconfigurable intelligent surfaces in real-world environment. *IEEE Open Journal of the Communications Society* **3**, 462–474.



Mehmet Ahad Yurtoglu received his Bachelor's degree in Electrical and Electronics Engineering from Gazi University, Türkiye, in 2021. In 2023, he received his Master of Science (M.Sc.) degree with cum laude in Telecommunication Engineering from Politecnico di Milano, Italy. Currently, he is a research associate at Fraunhofer HHI. He is interested in antennas, antenna arrays, microwave filters, filtering antennas, and reconfigurable intelligent surfaces.



Ramez Askar (IEEE SM) received his B.Eng. in 2008 from Homs (formerly AL-Baath) University, his M.Sc. in 2013 from Ilmenau University of Technology, and his Ph.D. (*summa cum laude*) in 2022 from Technische Universität Berlin. He is the deputy head of the mmWave Research group at Fraunhofer HHI. His research interests include full-duplex, self-interference channels and cancellation, transceiver hardware impairments, and sub-THz RF system design and propagation. He has published numerous peer-reviewed papers, journals, and patents – some of which are licensed – in his area of expertise. He received the Best Paper Award at IEICE SmartCom 2017 and the Best Demo awards at the 2024 IEEE 6G Summit in Dresden and the 2024 IEEE 6G Summit in Brooklyn.



Sven Wittig received B.Sc. and M.Sc. in electrical engineering from RWTH Aachen University in 2014 and 2016, respectively. Since 2017, he has been with the mmWave group at the Fraunhofer HHI. His main areas of interest are RF measurement systems and instrumentation, with a focus on wireless propagation channels and prototyping of broadband communication systems.



Mathis Schmieder received B.S. and M.S. in Electrical Engineering from Technische Universität Berlin in 2012 and 2017, respectively. Since then, he has been with the Fraunhofer HHI. He is also currently pursuing his Ph.D. at TU Berlin. His main research interests include millimeter-wave communications, measurement and modeling of wireless propagation channels, and wireless systems and transceiver architectures with emphasis on RF and analog circuit design.



Michael Peter received Dipl.-Ing. (M.S.) from the University of Karlsruhe in 2004 and Dr.-Ing (Ph.D.) from the Technische Universität Berlin in 2018. He is the head of the mmWave research group at Fraunhofer HHI. His research interests include millimeter-wave and THz communications with a focus on channel measurements and modeling, physical layer design and simulation, and performance analysis taking into account hardware impairments. He is an author and co-author of more than 80 peer-reviewed scientific papers.

https://doi.org/10.1017/S1759078726103341 Published online by Cambridge University Press